Chemistry–A European Journal
Research Article
doi.org/10.1002/chem.202404092
Chemistry Europe
European Chemical Societies Publishing
www.chemeurj.org

Sn(IV) Complexes of 5,10,15,20-Tetraaryl-5,15-diazaporphyrinoids: A Promising Platform for Evaluating the 20π-Electron Antiaromaticity

Hiroya Suzuki,[b] Mao Minoura,[c] Ko Furukawa,[d] Haruyuki Nakano,[e] and Yoshihiro Matano*[a]

Porphyrinoids in the 20π-electron state have been extensively studied from the fundamental viewpoint of investigating their structure–antiaromaticity relationships. However, most of the 20π porphyrinoids are highly distorted and unstable in air, which hinder the comprehensive analysis of paratropic ring-current effects derived from planar π-electron systems. Herein, we present the first examples of antiaromatic Sn(IV) complexes of 5,10,15,20-tetraaryl-5,15-diazaporphyrinoids (SnX_2TADAPs), prepared by the complexation of the corresponding freebases with Sn(II) chloride under aerobic conditions and subsequent metathesis of the axial ligands, that show paratropic ring-current effects. Notably, both neutral 20π-electron derivatives and 19π-electron radical cations of SnX_2TADAP are extremely stable in air owing to the intrinsic electronic effects of the central Sn(IV) unit and *meso* nitrogen atoms. NMR spectroscopy, cyclic voltammetry, and density functional theory calculations were performed to assess the ring-current effects and orbital energies of a series of the 20π-electron SnX_2TADAPs, and the results reveal that the paratropic ring-current effects arising from the planar 20π-electron DAP ring increases with a decrease in the HOMO–LUMO energy gap.

Introduction

Porphyrins are well known aromatic macrocycles that complex with metal ions, and their 18π-electron platforms have been widely used for constructing various functional dyes, semiconductors, and metal catalysts. In contrast, 20π porphyrins, the 2e-reduced species of regular porphyrins, are inherently antiaromatic macrocycles, and their structure–property relationship has long been a subject of interest for understanding the key factors that govern their antiaromaticity and optical properties.[1] To avoid the use of extremely air- and moisture-sensitive porphyrin dianions, several elaborate strategies have been adopted to isolate neutral 20π-electron porphyrinoids, including *N*-alkylation,[2] core modification with chalcogen and/or phosphorus atoms,[3,4] complexation with main-group elements,[5] and peripheral substitution of the porphyrin ring with strongly electron-withdrawing groups[6] or multiple aryl groups.[7] These approaches were developed to energetically stabilize the highest occupied molecular orbital (HOMO) and lowest unoccupied molecular orbital (LUMO) of the 20π-electron system by creating an isophlorin circuit. For example, Vaid et al. reported hexacoordinate Si(IV) and Ge(IV) complexes of 5,10,15,20-tetraphenylporphyrin (TPP; **P1**),[5a,b] in which the metal center was coordinated by the significantly ruffled isophlorin-type tetraanionic N_4-ligand. Owing to the paratropic ring-current effects originating from the isophlorin circuit, the ^{1}H NMR spectra of **P1** had upfield-shifted signals of pyrrolic-β protons ($C_β$-H) and downfield-shifted signals of axial pyridine ring protons. However, most of the isophlorin-type 20π-electron systems, excepting a few examples,[3a,c,6b] are highly distorted, making quantitative and systematic evaluation of the paratropic ring-current effects difficult. In addition, some derivatives are sensitive to air and moisture. Therefore, it is important to develop chemically stable and highly planar platforms for evaluating the antiaromaticity of 20π porphyrinoids.

Apart from these isophlorin derivatives, several types of 20π azaporphyrinoids with nitrogen atoms at the *meso* positions have been reported, and their antiaromatic characters have been discussed in terms of the ring-current effects estimated by NMR spectroscopy and theoretical calculations.[8–10] For example, Muranaka et al. reported weak paratropic ring-current effects of hemiporphyrazines[8a] and benzitetraazaporphyrin[8b] as 20π-electron systems, while Shinokubo et al. reported strong paratropic ring-current effects of 10,20-diaryl-5,15-dihydro-5,15-diazaporphyrinoid (**P2**).[9a] Our group has independently reported metal complexes of 5,10,15,20-tetraaryl-5,15-diazaporphyrinoid (MTADAP; **P3**) that were readily obtained by the

[a] *Prof. Dr. Y. Matano*
Department of Chemistry, Faculty of Science,
Niigata University, Nishi-ku, Niigata 950-2181 (Japan)
E-mail: matano@chem.sc.niigata-u.ac.jp
[b] *H. Suzuki*
Department of Fundamental Sciences, Graduate School of Science and Technology
Niigata University, Nishi-ku, Niigata 950-2181 (Japan)
[c] *Prof. Dr. M. Minoura*
Department of Chemistry, College of Science
Rikkyo University, Toshima-ku, Tokyo 171-8501 (Japan)
[d] *Prof. Dr. K. Furukawa*
Center for Coordination of Research Facilities, Institute for Research Administration
Niigata University, Nishi-ku, Niigata 950-2181 (Japan)
[e] *Prof. Dr. H. Nakano*
Department of Chemistry, Graduate School of Science,
Kyushu University, Nishi-ku, Fukuoka 819-0395 (Japan)

Supporting information for this article is available on the WWW under https://doi.org/10.1002/chem.202404092

metal-templated cyclization of the corresponding metal–bis(dipyrrin) complexes.[11] Recently, our group also established a general method for the synthesis of a freebase (H_2TADAP) and its conversion to a difluorosilicon(IV) complex (SiF_2TADAP).[12] In contrast to the air-sensitive *meso*-N–H derivatives, most of the 20π-electron derivatives of **P3** are air stable in the solid state. It should also be noted that **P3** provides the same flat π-network consisting of 18 C–C/C–N bonds of the DAP ring (bold line in Figure 1) to form the 20π-, 19π-, and 18π-electron systems through the participation of two lone electron pairs on the *meso*-N atoms in the HOMO and LUMO. Considering these characteristics, we prepared doubly strapped NiTADAP derivatives and investigated the intrinsic ring-current effects on their alkyl-chain straps.[11d] However, these derivatives were unsuitable for assessing the subtle differences in the electronic effects of the peripheral substituents and central metal atom.

Hexacoordinate group 14 metal(IV) complexes of porphyrins are well suited to experimentally investigate the ring-current effects, because their central metal in these complexes can also be exploited as probes for multinuclear NMR spectroscopy.[13,14] Furthermore, the HOMO and LUMO levels can be fine-tuned by changing the central metal and axial ligands. Herein, we report the first instances of hexacoordinate Sn(IV) complexes of TADAP with different axial ligands and *meso* substituents (SnX_2TADAP; X = axial ligands) synthesized from the corresponding H_2TADAP and Sn(II) chloride. The optical and electrochemical properties and antiaromatic character of SnX_2TADAP derivatives are discussed based on both experimental and theoretical results.

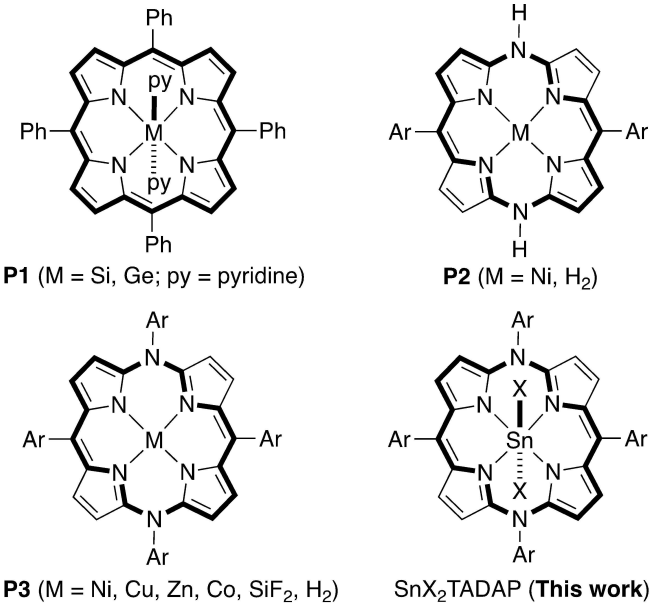

Figure 1. Selected examples of 20π porphyrinoids.

Results and Discussion

Figure 2 summarizes the structures of freebases and Sn(IV) complexes of 20π-electron TADAP, and Scheme 1 depicts the syntheses of 20π- and 19π-electron SnX_2TADAP derivatives. Freebases **1a**, **1b**, and **1c** were prepared according to previously reported methods.[11,12] The Sn(IV) complexes were synthesized as follows: a mixture of **1a**, $SnCl_2{\cdot}2H_2O$, and pyridine was refluxed under aerobic conditions and then treated with an aqueous HCl solution to obtain $SnCl_2$TADAP **2a-Cl**. Subsequently, **2a-Cl** was converted to several derivatives by the metathesis of the axial chlorine ligands with other anions. In brief, heating a mixture of **2a-Cl** and excess K_2CO_3 in THF/H_2O resulted in metathesis, furnishing $Sn(OH)_2$TADAP **2a-OH**. The subsequent reaction of **2a-OH** with an aqueous HF solution in a Teflon container yielded SnF_2TADAP **2a-F**. Finally, the reaction of **2a-Cl** with phenol, 4-chlorophenol, 4-nitrophenol, and 4-methoxyphenol under basic conditions in refluxing toluene afforded $Sn(OAr)_2$TADAP **2a-OAr^1**, **2a-OAr^2**, **2a-OAr^3**, and **2a-OAr^4**, respectively. The metathesis of **2a-Cl** with benzoic acid was realized in the presence of K_2CO_3 in toluene to obtain $Sn(OBz)_2$TADAP **2a-OBz**. The same protocol was used to synthesize **2b-X** and **2c-X** (X = Cl, F, and OH) from **1b** and **1c**, respectively. The one-electron oxidation of **2a,b,c-X** with $AgPF_6$ in CH_2Cl_2 yielded the corresponding 19π-electron radical cations, **3a,b,c-X**, as air-stable solids. However, 18π-electron dications, produced by the two-electron oxidation of **2a-X**,

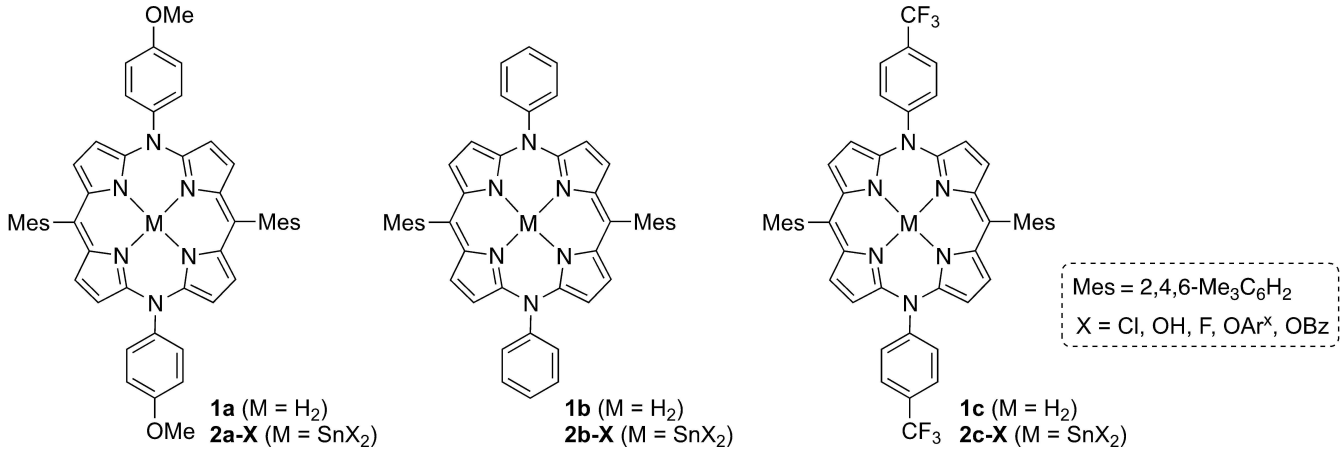

Figure 2. Structures of 20π-electron TADAP freebases **1a,b,c** and Sn(IV) complexes **2a,b,c-X**.

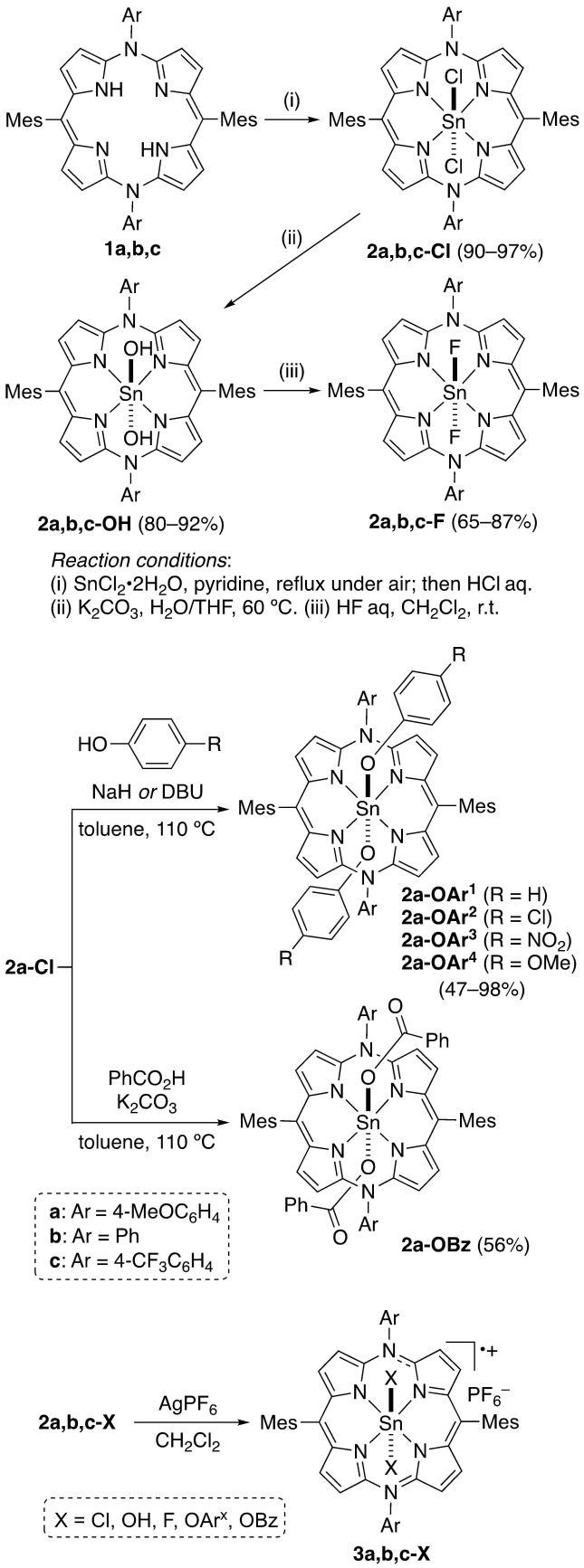

Scheme 1. Syntheses of SnX_2TADAP derivatives **2-X** and **3-X**.

could not be isolated because of their facile reduction to radical cations under ambient conditions.

The isolated SnX_2TADAP derivatives were characterized using NMR spectroscopy, high-resolution mass spectrometry (HRMS), and X-ray crystallography. In the HRMS profiles, intense peaks corresponding to $[M]^+$ and $[M - PF_6]^+$ ions were detected for only a few samples, reflecting the labile nature of the axial ligands in the ionization process.

Figure 3 depicts the crystal structures and selected bond lengths of **2a-Cl**, **2a-F**, **2c-F**, and **2a-OAr**[1]. In each compound, the Sn(IV) center adopted an octahedral geometry with the two halogen (Cl or F) or oxygen atoms located at axial positions. All compounds were found to have highly planar DAP rings with root-mean-square deviations (Δd_{RMS}) of 0.030–0.058 Å. The *meso*-aryl groups were almost perpendicular to the DAP ring (dihedral angles are 75.7–89.4°), suggesting negligible π-conjugation between them (Figures S1–S4). The average values

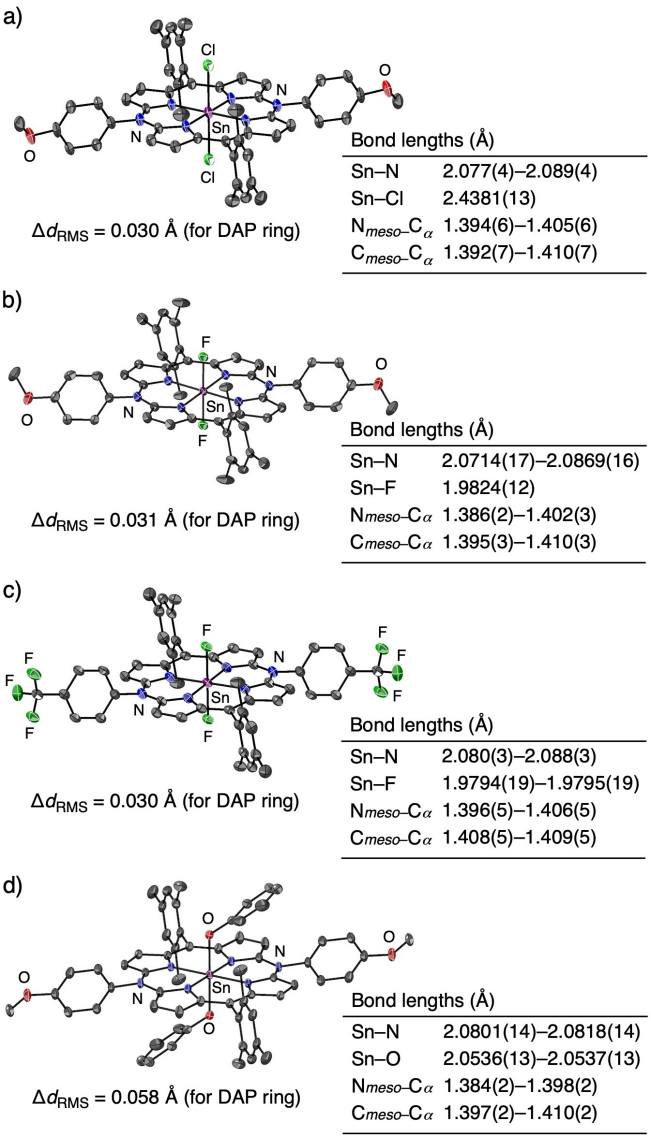

Figure 3. ORTEP diagrams (50% probability ellipsoids), selected bond lengths, and root-mean-square deviations (Δd_{RMS}) of a) **2a-Cl**, b) **2a-F**, c) **2c-F**, d) **2a-OAr**[1]. Hydrogen atoms are omitted for clarity.

of the harmonic oscillator model of aromaticity (HOMA)[15] determined from 18 C–X (X = C, N) bonds that make up the 20π-electron network are 0.762–0.807, which are somewhat smaller than the value calculated for the previously reported 20π-electron NiTADAP **P3** (M = Ni; HOMA = 0.837). These data suggest that **2-X** has a more significant antiaromatic character than NiTADAP in terms of the geometrical criterion. Furthermore, **2a-Cl** has a slightly long Sn–Cl bond length (2.438 Å) but a slightly short Sn–N bond length (2.083 Å) compared with those in $SnCl_2TPP$ (Sn–Cl: 2.420 Å; Sn–N: 2.098 Å).[16] This is likely due to the core size of the DAP ligand, which is contracted relative to that of porphyrin. The plot of the Sn–N bond length vs. pK_a of the conjugate acid of X for a series of hexacoordinate Sn(IV) complexes of TPP (SnX_2TPP) evidently reveals the effect of ligand basicity on the Sn–N bond length; the smaller the pK_a of HX is, the shorter the Sn–N bond length is.[17] However, no notable difference was observed in the Sn–N bond lengths of **2a-Cl**, **2a-F**, **2c-F**, and **2a-OAr^1** (~2.08 Å).

Figure 4 presents the ^{1}H NMR spectra of **2a-Cl**, **2a-F**, and **2a-OAr^1**, in which the $C_{\beta1}$–H/$C_{\beta2}$–H signals are observed at 3.30/2.23, 3.34/2.29, and 3.31/2.01 ppm, respectively, and the axial phenoxy-H signals of **2a-OAr^1** are observed at 11.1 (*ortho*), 8.27 (*meta*), and 7.65 (*para*) ppm.[18] The observed upfield and downfield shifts of the proton signals are due to the paratropic ring-current effects derived from the 20π-electron DAP ring, indicating the antiaromatic character of **2-X**. The $C_{\beta1}$–H/$C_{\beta2}$–H signals of **2a-F** (3.66/2.46 ppm in C_6D_6) were more shielded than those of previously reported 20π-electron MTADAP derivatives **P3** with the same *meso*-aryl groups (4.64/3.37 ppm for M = Ni; 4.07/3.02 ppm for M = Zn; and 4.66/3.32 ppm for M = SiF_2 in C_6D_6). The ^{119}Sn-NMR signals of **2a-X** (X = Cl, F, OBz, and OH) appeared downfield relative to the corresponding signals of SnX_2TPP; differences in chemical shifts ($\Delta\delta_{Sn}$) were 47.9–57.9 ppm.[19] These NMR data also reflect the effects of the paratropic ring current on the Sn nucleus in the 20π-electron SnX_2TADAP. The effects of the axial ligands, *meso*-substituents, and central metal atom on the ring current will be discussed later.

The experimentally acquired and simulated electron paramagnetic resonance (EPR) spectra of **3a-Cl** are shown in Figure 5. The hyperfine-coupling structure observed for **3a-Cl** and the electron spin densities calculated for **3m-Cl** revealed that the unshared electron of the π-cation radical was efficiently delocalized over the entire DAP ring.

The UV/Vis/NIR absorption spectra of **1**, **2-X**, and **3-X** in CH_2Cl_2 are shown in Figures 6 and S5, and their optical data are summarized in Table 1. The spectral features of **2-X** and **3-X** are similar to those of the known 20π- and 19π-electron MTADAP, respectively. For both **2-X** and **3-X**, the absorption maxima (λ_{max}) varied slightly depending on the axial ligands. To understand the orbital characteristics and the nature of electronic excitations in the SnX_2TADAP chromophores, we performed density

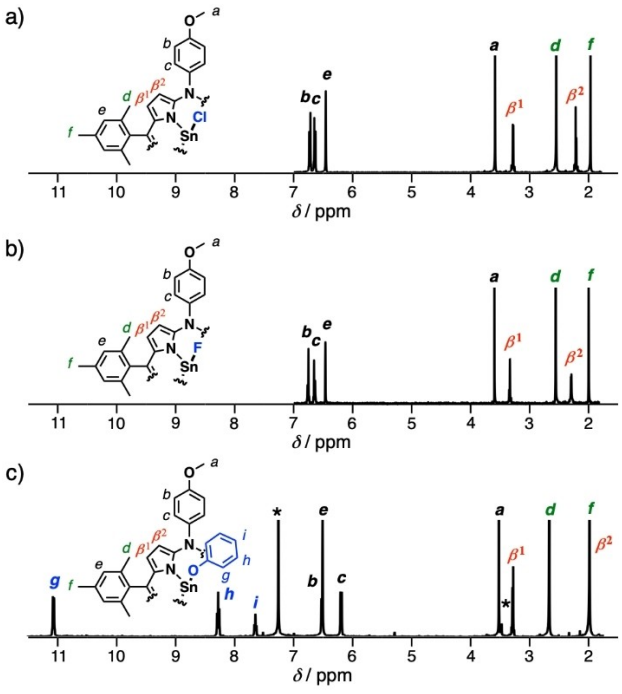

Figure 4. ^{1}H NMR spectra (400 MHz, $CDCl_3$) of a) **2a-Cl**, b) **2a-F**, c) **2a-OAr^1**. Asterisks indicate residual solvent peaks.

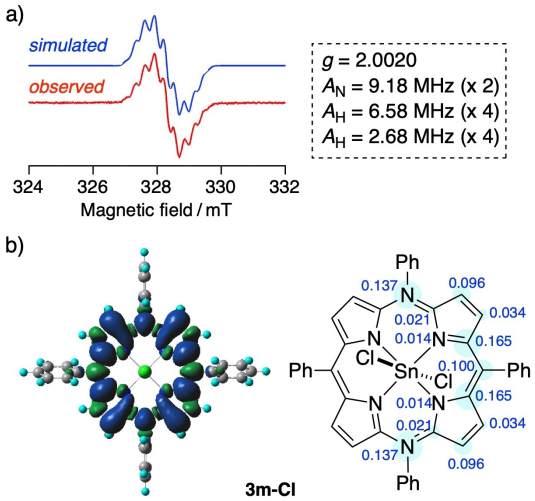

Figure 5. a) EPR spectra of **3a-Cl** observed in CH_2Cl_2 (red) and simulated (blue). b) Spin-density distribution at the optimized structure (left) and electron spin densities at the DAP ring (right) of **3m-Cl**; calculated by the DFT method.

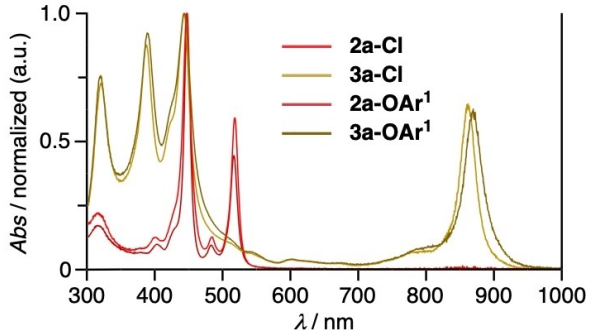

Figure 6. UV/Vis/NIR absorption spectra of **2a-Cl**, **3a-Cl**, **2a-OAr^1**, and **3a-OAr^1** in CH_2Cl_2.

Table 1. Optical and electrochemical data for SnX_2TADAPs in CH_2Cl_2.

TADAP	λ_{max}/nm (log ε)[a]	E/V[b]	$\Delta E_{H\text{-}L}$[c]
1a[d]	426 (4.80), 488 (4.53)	−1.99, −0.42, +0.21	1.57
1b	425 (4.72), 488 (4.45)	−2.02, −0.43, +0.21	1.59
1c	425 (4.98), 486 (4.73)	−1.93, −0.30, +0.28	1.63
2a-Cl	446 (5.21), 516 (4.86)	−1.49,[e] −0.08, +0.73	1.43[f]
2b-Cl	445 (5.20), 515 (4.84)	−1.49,[e] −0.06, +0.74	1.43
2c-Cl	445 (5.24), 512 (4.90)	−1.43,[e] +0.05, +0.83	1.48
2a-F	443 (5.15), 516 (4.76)	−1.56, −0.11, +0.70	1.45
2b-F	442 (5.30), 513 (4.90)	−1.56, −0.11, +0.70	1.45
2c-F	441 (5.27), 510 (4.89)	−1.49, 0.00, +0.77	1.49
2a-OH	444 (5.27), 516 (4.91)	−1.63, −0.18, +0.58	1.45
2b-OH	443 (5.20), 514 (4.82)	−1.62, −0.18, +0.48	1.44
2c-OH	443 (5.27), 512 (4.93)	−1.54, −0.08, +0.54	1.46
2a-OBz	446 (5.27), 517 (4.90)	−1.60, −0.15	1.45
2a-OAr^1	446 (5.34), 517 (5.09)	−1.63, −0.16	1.47
2a-OAr^2	446 (5.21), 517 (4.97)	−1.56, −0.10	1.46
2a-OAr^3	446 (5.33), 515 (4.97)	−1.46, +0.02, +0.80	1.48
2a-OAr^4	445 (5.25), 517 (4.95)	−1.62, −0.16	1.46
3a-Cl	386 (4.67), 442 (4.73), 863 (4.54)		
3b-Cl	385 (4.55), 443 (4.72), 862 (4.46)		
3c-Cl	385 (4.53), 440 (4.71), 872 (4.42)		
3a-F	386 (4.77), 442 (4.82), 866 (4.68)		
3b-F	385 (4.61), 442 (4.79), 867 (4.55)		
3c-F	384 (4.75), 440 (4.93), 873 (4.64)		
3a-OH	386 (4.68), 442 (4.74), 864 (4.56)		
3b-OH	385 (4.79), 442 (4.97), 867 (4.72)		
3c-OH	384 (4.66), 440 (4.83), 873 (4.53)		
3a-OBz	386 (4.79), 442 (4.85), 861 (4.64)		
3a-OAr^1	387 (4.80), 442 (4.83), 871 (4.63)		
3a-OAr^2	387 (4.89), 442 (4.95), 865 (4.77)		
3a-OAr^3	385 (4.78), 442 (4.83), 867 (4.67)		
3a-OAr^4	385 (4.78), 442 (4.84), 866 (4.66)		

[a] Absorption maxima (λ_{max}; >350 nm) and logarithm of molecular extinction coefficients (log ε >4). [b] Half-wave potentials (vs. Fc/Fc^+) of the reversible 21π/20π, 20π/19π, and 19π/18π redox couples unless otherwise noted. [c] $\Delta E_{H-L} = E_{(20\pi/19\pi)} - E_{(21\pi/20\pi)}$. [d] Data from ref. [9b]. [e] Irreversible processes: $E_{(21\pi/20\pi)}$ values were determined using DPV. [f] The $E_{(20\pi/19\pi)}$ value of −0.06 V, determined using DPV, was used for calculating ΔE_{H-L}.

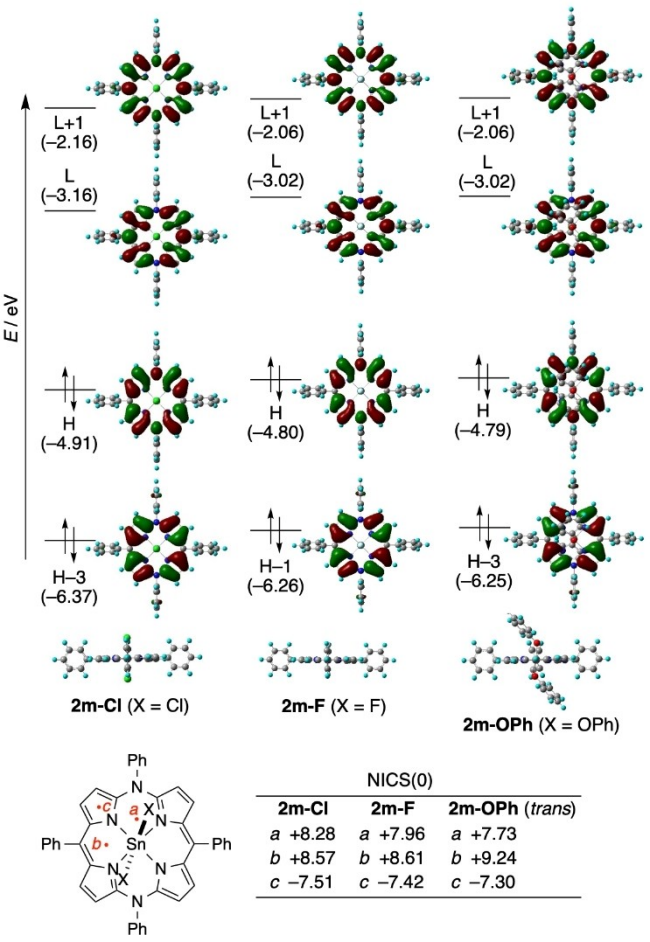

Figure 7. Selected Kohn-Sham orbitals and their energies of **2m-Cl**, **2m-F**, **2m-OPh** (*trans*) and NICS(0) values at three positions on the DAP ring of **2m-X**.

functional theory (DFT) calculations of model compounds **2m-X** (X = F, Cl, or OPh) (Figure 7) and **3m-Cl** (Figure 5). The HOMO and LUMO energies of **2m-F** and **2m-Cl** were lower than those of **2m-OPh**, reflecting the different electronic effects of the axial ligands. Time-dependent DFT (TD-DFT) calculations (Table S1) revealed that the HOMO-to-LUMO excitation of **2m-X** is symmetrically forbidden (oscillator strength is nearly equal to zero). Indeed, no clear absorption band due to the HOMO-to-LUMO excitation was detected above 550 nm for **2-X**. The intense visible band of **2-X** below 550 nm (λ_{max} = 510–517 nm; X = F, Cl, or OPh) is mainly due to the HOMO-to-LUMO+1 π–π* excitation, whereas the intense NIR band of **3-Cl** (λ_{max} = 863–872 nm) can be attributed to β-HOMO-to-β-SOMO π–π* excitation (SOMO = singly occupied molecular orbital).

The electrochemical properties of **1** and **2-X** in CH_2Cl_2 were evaluated through cyclic voltammetry (CV) and differential pulse voltammetry (DPV) using Bu_4NPF_6 as a supporting electrolyte. The voltammograms are shown in Figures 8 and S6, and the redox potentials (E) vs. ferrocene/ferrocenium couple (Fc/Fc^+) are listed in Table 1. The 21π/20π and 20π/19π redox processes of SnX_2TADAPs occurred in the potential ranges of −1.63 to −1.46 V and −0.18 to +0.05 V, respectively. For some derivatives, the 19π/18π redox process was clearly observed in the relatively positive potential range (E > +0.54 V), reflecting the highly electron-accepting character of the 18π-electron dications of SnX_2TADAPs (*vide supra*). The redox potentials of **2a-X** were considerably shifted to the positive side relative to those of previously reported **P3** (M = Zn, Ni, Cu, and SiF_2) with the same *meso*-aryl groups,[11,12] highlighting the strongly electron-withdrawing nature of the SnX_2 unit to stabilize the frontier orbitals of the DAP ring. Furthermore, the electrochemical HOMO–LUMO gaps ($\Delta E_{H\text{-}L}$) of the 20π-electron MTADAP decreased in the order of H_2TADAP **1a** (1.57 V) >

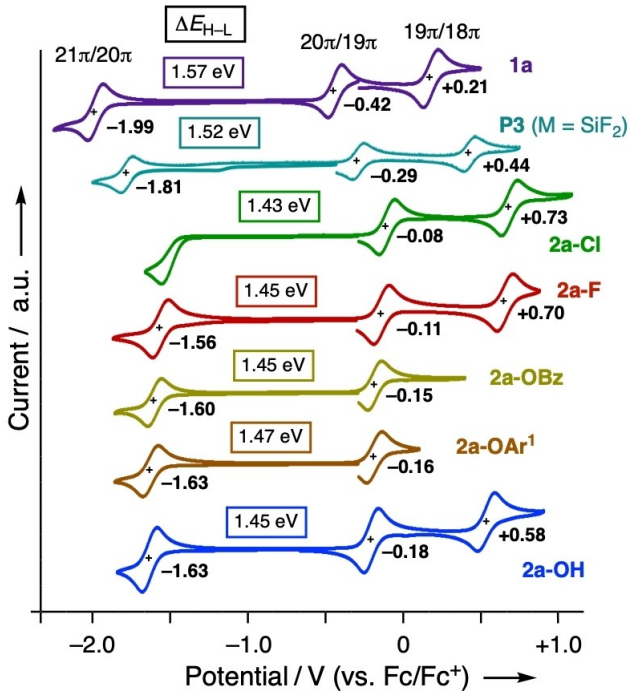

Figure 8. Cyclic voltammograms of **1a**, **P3** (M = SiF_2), **2a-Cl**, **2a-F**, **2a-OBz**, **2a-OAr^1**, and **2a-OH**. Measured in CH_2Cl_2 with Bu_4NPF_6; scan rate = 60 mV s^{-1}. The half-wave potentials and $\Delta E_{H\text{-}L}$ are indicated. See also Table 1.

SiF_2TADAP **P3** (M = SiF_2; 1.52 V) > SnF_2TADAP **2a-F** (1.45 V). These data indicate that Sn(IV) is more effective than Si(IV) for constructing 20π-electron azaporphyrinoids with a smaller $\Delta E_{H\text{-}L}$. As shown in Figure 8, the 20π/19π and 20π/21π redox processes of **2a-X** shifted to the positive side in the order of **2a-OH**, **2a-OAr^1**, **2a-OBz**, **2a-F**, **2a-Cl**, which unambiguously reflects the order of the pK_a of the corresponding conjugate acids (HX; X = OH, OPh, OCOPh, F, Cl) of the axial ligands. Thus, the HOMO and LUMO energies of **2a-X** increased as the basicity of the axial ligand increased, which can allow the redox potentials and $\Delta E_{H\text{-}L}$ of the 20π-electron DAP ring to be fine-tuned. Among the aryloxy-substituted derivatives, the redox processes shifted to the positive side in the order of **2a-OAr^1**, **2a-OAr^4** < **2a-OAr^2** < **2a-OAr^3**, also reflecting the electronic effect of the *para*-substituents of their axial ligands (H, OMe, Cl, NO_2) on the HOMO and LUMO energies. However, the $\Delta E_{H\text{-}L}$ of **2a-X** (1.43–1.48 V) was only slightly altered by the axial ligands; consequently, no clear correlation could be established between the base strength of axial ligands and $\Delta E_{H\text{-}L}$. The *para*-substituents on the *N*-aryl groups also affected the redox potentials. When the axial ligands were the same, the *E* values of *p*-CF_3 derivatives **2c-X** were positively shifted relative to those of *p*-H derivatives **2a-X** and *p*-OMe derivatives **2b-X**. The substituent effects of the *meso*-*N*-aryl groups had a more pronounced effect on the 20π/19π redox couple than on the 21π/20π redox couple. Consequently, the $\Delta E_{H\text{-}L}$ of **2c-X** (1.46–1.49 eV) were appreciably larger than those of **2a-X** and **2b-X** (1.43–1.45 eV) with the same axial ligands. The small differences between the $\Delta E_{H\text{-}L}$ of **2a-X** and **2b-X** are probably due to the suppression of the resonance effect of the *p*-OMe group by the vertical orientation of the *meso*-*N*-aryl rings.

As mentioned above, **2-X** have the highly planar 20π-electron conjugated circuits that are difficult to construct with isophlorin-type porphyrinoids. When an antiaromatic compound with a small $\Delta E_{H\text{-}L}$ is placed in a magnetic field, the paramagnetic term in the NMR shielding constant formulation gains in importance to chemical shifts (δ) owing to mixing of the excited-state and ground-state wavefunctions.[20] Thus, the paratropic ring-current effects observed by NMR spectroscopy have been used as a measure of the antiaromaticity of cyclic π-conjugated molecules with 4n π electrons; the smaller the $\Delta E_{H\text{-}L}$ is, the larger the paratropic ring-current effect is. Table S2 summarizes the correlations between the $\Delta E_{H\text{-}L}$ and NMR chemical shifts of several protons of **2-X** and the related 20π-electron TADAP. Figures 9a and 9b show the plots of $(\Delta E_{H\text{-}L})^{-1}$ versus the upfield shifts ($\Delta\delta_H$) of the C_β–H signals of **2-X** relative to those of the corresponding dipyrrin precursors **4a,b,c**[21] (dipyrrin-ref; in Table S2), and Figure 9c shows the plots of $(\Delta E_{H\text{-}L})^{-1}$ versus the ^{119}Sn chemical shifts (δ_{Sn}) of **2a,b,c-X** (X = F, Cl, OH). Further, the plots of $(\Delta E_{H\text{-}L})^{-1}$ versus $\Delta\delta_H$ of the *ortho*- and *para*-methyl signals of **2a,b,c-X** are shown in Figure S7. The nuclear-independent chemical shift (NICS)[22] values calculated

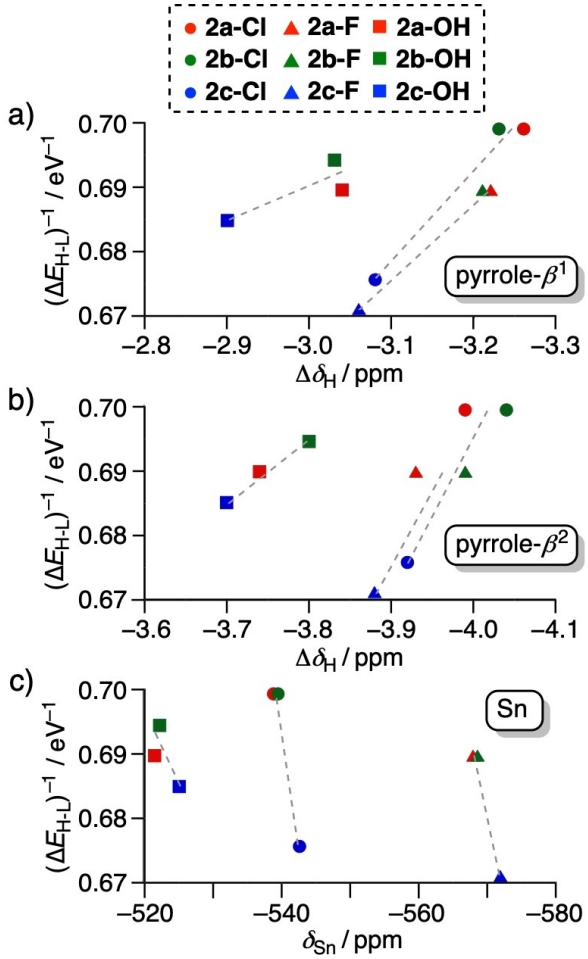

Figure 9. Plots of $(\Delta E_{H\text{-}L})^{-1}$ vs. a) $\Delta\delta_H$ of $C_{\beta1}$-H, b) $\Delta\delta_H$ of $C_{\beta2}$-H, and c) δ_{Sn} of **2a-X**, **2b-X**, and **2c-X** (X = Cl, F, and OH).

for three positions in the π-plane of the corresponding models, i.e., **2m-X** are listed in Figure 7. With these data, the relationship between the $\Delta E_{H\text{-}L}$ and paratropic ring-current effects on the ^{1}H and ^{119}Sn nuclei are discussed. First, the effects of the axial ligands on the $\Delta E_{H\text{-}L}$ and $\Delta\delta_H$ are compared using the data for **2a-X** with the same *meso*-aryl groups. The $\Delta E_{H\text{-}L}$ of **2a-X** ranged from 1.43 to 1.48 eV, while the $\Delta\delta_H$ of the peripheral $C_{\beta1}$–H and $C_{\beta2}$–H signals ranged from −3.04 to −3.30 ppm and −3.74 to −4.21 ppm, respectively. As shown in Figure S7a, no clear correlation could be established between the $(\Delta E_{H\text{-}L})^{-1}$ and $\Delta\delta_H$ for the **2a-X** series. This is partly due to the non-negligible influence of the through-space anisotropic effects of the axial ligands on the C_β–H signals of **2a-X**. For example, the relatively large upfield shifts of the C_β–H signals of **2a-OAr**[1] compared with those of **2a-OH** are attributable to additional shielding effects derived from their axial phenoxy ligands. This was further supported by the NICS calculations of **2m-OPh** (Figure S8). The NICS(0) values for positions *a* and *b* of the *cis* conformer and for positions *a*, *b*, and *e* of the *trans* conformer differed considerably, indicating that the local ring currents derived from the tilted benzene rings in the axial ligands contributed to the overall shielding effects on the C_β–H signals.

We next compared the effects of the *meso*-*N*-aryl groups using the data for compounds with the same axial ligands, viz., **2a-X**, **2b-X**, and **2c-X** (X = F, Cl, OH). As mentioned above, the $\Delta E_{H\text{-}L}$ values of **2c-X** ($\Delta E_{H\text{-}L}$ = 1.46–1.49 eV) were larger than those of **2a-X** and **2b-X** ($\Delta E_{H\text{-}L}$ = 1.43–1.45 eV). A clear correlation was found between the $\Delta E_{H\text{-}L}$ and $\Delta\delta_H$ for each SnX_2TADAP; the smaller the $\Delta E_{H\text{-}L}$ was, the larger the absolute $\Delta\delta_H$ was. The plots in Figures 9a,b and S7b,c reveal that the shielding effects on the C_β-H and *para*-Me signals and the deshielding effects on the *ortho*-Me signals observed for **2a-X** and **2b-X** are greater than the corresponding effects observed for **2c-X**. These results are consistent with the prediction that the paratropic ring-current effects arising from the antiaromatic 20π-electron porphyrin rings increase with increasing the $(\Delta E_{H\text{-}L})^{-1}$ value. The ^{119}Sn-NMR and ^{19}F-NMR signals of **2a-X** and **2b-X** appeared downfield compared with those of **2c-X** (X = Cl, F, and OH). As the differences in the ^{19}F–^{119}Sn coupling constants of the 20π-electron SnF_2TADAP are small ($J_{F\text{-}Sn}$ = 1796 Hz for **2a-F**, 1797 Hz for **2b-F**, and 1802 Hz for **2c-F**), the differences in the δ_{Sn} and δ_F values mainly reflected the different paratropic ring-current effects of **2a-F**, **2b-F**, and **2c-F**. These data provide clear evidence of the relationship between the antiaromatic character of the DAP ring and $\Delta E_{H\text{-}L}$.

Finally, the effects of the central metal units were compared using the data for **2a-F** and SiF_2TADAP (**P3-SiF$_2$**; M = SiF_2) with the same axial ligands and *meso*-aryl groups. As listed in Table S2, the degree of the shielding/deshielding effects on the C_β-H, *para*-Me, and *ortho*-Me signals of **2a-F** was greater than that of **P3-SiF$_2$**. As shown in Figure 8, the 21π/20π and 20π/19π redox potentials of **2a-F** were positively shifted relative to the corresponding potentials of **P3-SiF$_2$** by 0.25 V and 0.18 V, respectively, reflecting the different electronegativities of Sn (1.96) and Si (1.90). The $\Delta E_{H\text{-}L}$ of **2a-F** (1.45 eV) was smaller than that of **P3-SiF$_2$** (1.52 eV), suggesting that the $\Delta E_{H\text{-}L}$ is the main factor that affects the degree of paratropic ring-current effects arising from the 20π-electron DAP rings contained in these group 14 metal(IV) complexes. The NICS(0) values calculated for positions *a* and *b* of Sn-model complex **2m-F** (+7.96 and +8.61 ppm) are more positive than the corresponding values of Si-model complex **P3-SiF$_2$** (+6.82 and +7.09 ppm). This result also substantiates the aforementioned relationship between the $\Delta E_{H\text{-}L}$ and paratropic ring-current effects arising from the 20π DAP rings (Figure S9).

Conclusions

Several Sn(IV) complexes of TADAPs (SnX_2TADAPs) in the 20π- and 19π-electron states were synthesized by the complexation of the corresponding freebases with $SnCl_2{\cdot}2H_2O$, followed by the metathesis of the axial ligands and subsequent redox reactions of the DAP rings. The neutral 20π-electron derivatives were extremely air stable and contained highly planar DAP rings, which are favorable for assessing their antiaromatic characters in terms of magnetic and geometrical criteria. The 19π-electron cation radicals were also air stable owing to the efficient delocalization of the electron spin over the DAP ring. The shielding/deshielding effects arising from the 20π-electron circuit of SnX_2TADAPs were investigated using NMR spectroscopy and DFT calculations. When the chemical shifts of the C_β–^{1}H and ^{119}Sn nuclei were used as the indicators of the paratropic ring-current effects, the additional local anisotropic effects derived from the axial ligands should be considered. The comparison of the data obtained for a series of 20π-electron SnX_2TADAPs with the same axial ligands but different *meso*-*N*-substituents indicated that the paratropic ring-current effect of the 20π-electron system increases as the HOMO–LUMO gap of the complex decreases. This study not only provides valuable information on the antiaromaticity of highly planar 20π-electron porphyrinoids, but also demonstrates that SnX_2TADAP is a promising platform to experimentally quantify paratropic ring-current effects. Further studies on TADAP-based metal complexes in the 20π-electron state are currently underway in our laboratory.

Experimental Section

General Remarks: All melting points were recorded on a micro melting point apparatus and are uncorrected. The NMR spectra were recorded on 400 MHz (Agilent) and 700 MHz (Bruker) spectrometers. The ^{1}H and ^{13}C chemical shifts are reported in ppm as relative values vs. Me_4Si (0 ppm in $CDCl_3$) or a solvent residual signal (7.16 ppm in C_6D_6). The ^{19}F chemical shifts are reported in ppm vs. $CFCl_3$ (0 ppm), and the ^{119}Sn chemical shifts are reported in ppm vs. Me_4Sn (0 ppm). High-resolution mass (HRMS) spectra were measured on Thermo Fisher Scientific EXACTIVE (electron spray–quadrupole; ESI) and Bruker Autoflex III smartbeam (matrix assisted laser desorption/ionization–time of flight; MALDI-TOF) spectrometers. The UV/Vis/NIR absorption spectra were measured on JASCO V-530 and V-730 spectrometers. The IR (Attenuated Total Reflection; ATR) spectra were obtained on a JASCO FT/IR4600 spectrometer. Redox potentials were measured at room temperature on an ALS model 650E electrochemical workstation using a glassy carbon working electrode, a platinum wire counter electrode, and an Ag/

Ag^+ [0.01 M $AgNO_3$, 0.1 M Bu_4NPF_6 (MeCN)] reference electrode. Thin-layer chromatography was performed with Kieselgel 60 F254, and preparative column chromatography was performed using Silica Gel 60 spherical, neutrality. All reactions were performed under an argon atmosphere unless otherwise noted. Compounds **1a** and **1b** were prepared following a modified route of the previously reported method.[12] Other chemicals and solvents were of reagent grade quality and used without further purification unless otherwise noted. For the synthesis and all characterization data of new compounds are reported in the Supporting Information.

X-ray Crystallographic Analysis: Single crystals used for the measurements were grown from CH_2Cl_2–CH_3CN (for **2a-Cl** and **2c-F**) or $CHCl_3$–CH_3CN (for **2a-F** and **2a-OAr^1**) at room temperature. Deposition Numbers 2395473 (for **2a-Cl**), 2395474 (for **2a-F**), 2395475 (for 2**a-OAr^1**), 2395476 (for **2c-F**) contain the supplementary crystallographic data for this paper. These data are provided free of charge by the joint Cambridge Crystallographic Data Centre and Fachinformationszentrum Karlsruhe Access Structures service. Selected parameters are as follows. **2a-Cl**: $C_{50}H_{44}Cl_2N_6O_2Sn$, MW = 950.50, 0.100×0.100×0.010 mm, monoclinic, $P2_1/c$, a = 12.9344(16) Å, b = 12.9854(15) Å, c = 13.2816(16) Å, β = 104.975(4)°, V = 2155.0(4) Å^3, Z = 2, ρ_{calcd} = 1.465 g cm^{-3}, μ = 7.66 cm^{-1}, collected 52367, independent 4939, parameters 281, R_w = 0.1559 (all data), R_1 = 0.0548 ($I > 2.0\sigma(I)$), GOF = 1.188. **2a-F**: In terms of unit cell voids, PLATON/SQUEEZE has been applied to the highly disordered recrystallisation solvents CH_3CN and $CHCl_3$. $C_{50}H_{44}F_2N_6O_2Sn$, MW = 917.60, 0.100×0.100×0.050 mm, monoclinic, $P2_1/n$, a = 12.5047(10) Å, b = 14.4943(10) Å, c = 15.4490(12) Å, β = 111.982(2)°, V = 2596.5(3) Å^3, Z = 2, ρ_{calcd} = 1.174 g cm^{-3}, μ = 5.39 cm^{-1}, collected 61491, independent 5947, parameters 281, R_w = 0.0904 (all data), R_1 = 0.0317 ($I > 2.0\sigma(I)$), GOF = 1.074. **2c-F**: $C_{50}H_{38}F_8N_6Sn$, MW = 993.55, 0.010×0.010×0.010 mm, monoclinic, $P2_1/c$, a = 13.668(2) Å, b = 12.647(2) Å, c = 12.729(2) Å, β = 107.922(2)°, V = 2093.6(6) Å^3, Z = 2, ρ_{calcd} = 1.576 g cm^{-3}, μ = 8.13 cm^{-1}, collected 47209, independent 4800, parameters 298, R_w = 0.1548 (all data), R_1 = 0.0561 ($I > 2.0\sigma(I)$), GOF = 0.893. **2a-OAr^1**•$(CHCl_3)_2$: $C_{64}H_{56}Cl_6N_6O_4Sn$, MW = 1304.53, 0.010×0.010×0.010 mm, tetragonal, $I4_1/a$, a = 30.671(7) Å, b = 30.671(7) Å, c = 12.561(3) Å, V = 11816(6) Å^3, Z = 8, ρ_{calcd} = 1.467 g cm^{-3}, μ = 6.26 cm^{-1}, collected 136528, independent 6784, parameters 371, R_w = 0.0816 (all data), R_1 = 0.0297 ($I > 2.0\sigma(I)$), GOF = 1.031.

DFT Calculations: The geometries of model compounds were optimized with the density functional theory (DFT) method. The basis sets used for the optimization were 6–311G(d,p) basis set[23] for H, C, N, F, and Cl and the LANL08(d) basis set (with effective core potentials)[24] for Sn. The functional of DFT was the Becke, three-parameter, Lee–Yang–Parr (B3LYP) exchange-correlation functional.[25] The optimized geometries were confirmed to be minima by vibrational analysis. The Cartesian coordinates and computed total energies of **2m-X** and **3m-X** are summarized in Table S3. The excitation energies and oscillator strengths listed in Table S1 were computed with the time-dependent density functional theory (TD-DFT) method. The solvent effects were incorporated in both the DFT and TD-DFT calculations using the polarizable continuum model (PCM) with the integral equation formalism variant.[26] The nucleus-independent chemical shift (NICS)[14] were calculated at the Hartree–Fock level with gauge-including atomic orbitals (GIAOs) at the DFT optimized geometries. The basis sets used for the NICS calculations were the 6–31 + G(d) basis set[27] for H, C, N, F, and Cl and the LANL2DZdp basis set (with effective core potentials)[24] for Sn. The solvent effect was not included in the NICS and ACID calculations. All the calculations were carried out using the Gaussian 16 suite of programs.[28]

EPR Measurements. The electron paramagnetic resonance (EPR) spectrum of **3a-Cl** was measured at room temperature by using a JEOL JES-FA200 spectrometer equipped with an OXFORD ESR900 He-flow cryostat. A sample was prepared as a 0.1 mM solution in CH_2Cl_2. After three freeze-pump-thaw cycles, the solution sample in a quartz tube was sealed by frame. Spectral simulation was performed using EasySpin,[29] which is a MATLAB toolbox meant for this. The static magnetic field and microwave frequency were measured by an Echo Electronics EFM-2000 gauss meter and a TakedaRiken TR5212 microwave counter, respectively.

Acknowledgements

This work was supported by JSPS KAKENHI (23K23329 to YM, 21K04980 to HN) from MEXT, Japan. We would also like to express our gratitude to the SPring-8 synchrotron facility, where synchrotron-radiation experiments were performed at the BL02B1 beamlines with the approval of the Japan Synchrotron Radiation Research Institute (JASRI) under proposal numbers 22022B1603, 2023A1727, 2023B1682, and 2023B2038.

Conflict of Interests

The authors declare no conflict of interest.

Data Availability Statement

The data that support the findings of this study are available in the supplementary material of this article.

Keywords: Porphyrinoids · Diazaporphyrin · Dyes/Pigments · Antiaromaticity · Ring-current Effects

[1] a) G. L. Closs, L. E. Closs, *J. Am. Chem. Soc.* **1963**, *85*, 818–819; b) J. W. Buchler, L. Puppe, *Liebigs Ann. Chem.* **1970**, *740*, 142–163; c) R. Cosmo, C. Kautz, K. Meerholz, J. Heinze, K. Müllen, *Angew. Chem. Int. Ed. Engl.* **1989**, *28*, 604–607; *Angew. Chem.* **1989**, *101*, 638–640; d) E. Steiner, P. W. Fowler, *ChemPhysChem* **2002**, *3*, 114–116; e) K. M. Kadish, E. Van Caemelbecke, G. Royal, in *The Porphyrin Handbook*, Vol 8 (Eds.: K. M. Kadish, K. M. Smith, R. Guilard), Academic Press, San Diego, **2000**, pp. 1–114; f) J. I. Wu, I. Fernández, P. v R Schleyer, *J. Am. Chem. Soc.* **2013**, *135*, 315–321; g) S. Hiroto, H. Shinokubo, in *The Porphyrin Handbook*, Vol 37 (Eds.: K. M. Kadish, K. M. Smith, R. Guilard), Academic Press, San Diego, **2016**, pp. 233–302; h) B. K. Reddy, A. Basavarajappa, M. D. Ambhore, V. G. Anand, *Chem. Rev.* **2017**, *117*, 3420–3443; i) H. Fliegl, M. Dimitrova, R. J. F. Berger, D. Sundholm, *Chemistry* **2021**, *3*, 1005–1021; j) D. Sundholm, H. Fliegl, in *The Porphyrin Handbook*, Vol 46 (Eds.: K. M. Kadish, K. M. Smith, R. Guilard), Academic Press, San Diego, **2022**, pp. 1–39; k) Y. Matano, in *The Porphyrin Handbook*, Vol 46 (Eds.: K. M. Kadish, K. M. Smith, R. Guilard), Academic Press, San Diego, **2022**, pp. 41–111, and references therein.

[2] a) M. Pohl, H. Schmickler, J. Lex, E. Vogel, *Angew. Chem., Int. Ed. Engl.* **1991**, *30*, 1693–1697; *Angew. Chem.* **1991**, *103*, 1737–1741; b) J. Setsune, K. Kashihara, K. Wada, H. Shinozaki, *Chem. Lett.* **1999**, *28*, 847–848; c) T. P. Vaid, *J. Am. Chem. Soc.* **2011**, *133*, 15838–15841.

[3] a) J. S. Reddy, V. G. Anand, *J. Am. Chem. Soc.* **2008**, *130*, 3718–3719; b) M. Kon-no, J. Mack, N. Kobayashi, M. Suenaga, K. Yoza, T. Shinmyozu, *Chem. Eur. J.* **2012**, *18*, 13361–13371; c) B. K. Reddy, S. C. Gadekar, V. G. Anand, *Chem. Commun.* **2015**, *51*, 8276–8279; d) S. P. Panchal, S. C. Gadekar, V. G. Anand, *Angew. Chem. Int. Ed.* **2016**, *55*, 7797–7800; e) S. P.

Panchal, B. K. Reddy, V. G. Anand, *Synlett* **2018**, *29*, 2362–2371; f) P. Pushpanandan, M. Ravikanth, *Chem. Rec.* **2022**, *22*, e202200144.
[4] a) Y. Matano, T. Nakabuchi, S. Fujishige, H. Nakano, H. Imahori, *J. Am. Chem. Soc.* **2008**, *130*, 16446–16447; b) T. Nakabuchi, M. Nakashima, S. Fujishige, H. Nakano, Y. Matano, H. Imahori, *J. Org. Chem.* **2010**, *75*, 375–389; c) Y. Matano, T. Nakabuchi, H. Imahori, *Pure Appl. Chem.* **2010**, *82*, 583–593.
[5] a) J. A. Cissell, T. P. Vaid, A. L. Rheingold, *J. Am. Chem. Soc.* **2005**, *127*, 12212–12213; b) J. A. Cissell, T. P. Vaid, G. P. A. Yap, *J. Am. Chem. Soc.* **2007**, *129*, 7841–7847; c) A. Weiss, M. C. Hodgson, P. D. W. Boyd, W. Siebert, P. J. Brothers, *Chem. Eur. J.* **2007**, *13*, 5982–5993; d) P. J. Brothers, *Chem. Commun.* **2008**, 2090–2102.
[6] a) C. Liu, D.-M. Shen, Q.-Y. Chen, *J. Am. Chem. Soc.* **2007**, *129*, 5814–5815; b) H. Sugimura, K. Nakajima, K. Yamashita, T. Ogawa, *Eur. J. Org. Chem.* **2022**, *2022*, e202200747.
[7] W. Suzuki, H. Kotani, T. Ishizuka, Y. Shiota, K. Yoshizawa, T. Kojima, *Angew. Chem. Int. Ed.* **2018**, *57*, 1973–1977.
[8] a) A. Muranaka, S. Ohira, D. Hashizume, H. Koshino, F. Kyotani, M. Hirayama, M. Uchiyama, *J. Am. Chem. Soc.* **2012**, *134*, 190–193; b) A. Muranaka, S. Ohira, N. Toriumi, M. Hirayama, F. Kyotani, Y. Mori, D. Hashizume, M. Uchiyama, *J. Phys. Chem. A* **2014**, *118*, 4415–4424; c) S. Yanagi, A. Matsumoto, N. Toriumi, Y. Tanaka, K. Miyamoto, A. Muranaka, M. Uchiyama, *Angew. Chem. Int. Ed.* **2023**, *62*, e202218358; d) S. Yanagi, O. Takayama, N. Toriumi, A. Muranaka, D. Hashizume, M. Uchiyama, *Chem. Eur. J.* **2024**, *30*, e202400401.
[9] a) A. Yamaji, H. Tsurugi, Y. Miyake, K. Mashima, H. Shinokubo, *Chem. Eur. J.* **2016**, *22*, 3956–3961; b) T. Sakurai, Y. Hiraoka, H. Tanaka, Y. Miyake, N. Fukui, H. Shinokubo, *Angew. Chem. Int. Ed.* **2023**, *62*, e202300437.
[10] Besides azaporphyrinoids, 20π-electron 5,15-dioxaporphyrinoids have been reported by Shimizu and coworkers. For example, see: a) A. Nishiyama, M. Fukuda, S. Mori, K. Furukawa, H. Fliegl, H. Furuta, S. Shimizu, *Angew. Chem. Int. Ed.* **2018**, *57*, 9728–9733; b) A. Nishiyama, Y. Tanaka, S. Mori, H. Furuta, S. Shimizu, *J. Porphyr. Phthalocyanines* **2020**, *24*, 355–361.
[11] a) T. Satoh, M. Minoura, H. Nakano, K. Furukawa, Y. Matano, *Angew. Chem. Int. Ed.* **2016**, *55*, 2235–2238; b) K. Sudoh, T. Satoh, T. Amaya, K. Furukawa, M. Minoura, H. Nakano, Y. Matano, *Chem. Eur. J.* **2017**, *23*, 16364–16373; c) Y. Satoh, Y. Kudoh, K. Furukawa, Y. Matano, *Org. Lett.* **2022**, *24*, 3839–3843; d) H. Ochiai, K. Furukawa, H. Nakano, Y. Matano, *J. Org. Chem.* **2021**, *86*, 2283–2296.
[12] H. Suzuki, K. Furukawa, M. Minoura, H. Nakano, Y. Matano, *Bull. Chem. Soc. Jpn.* **2024**, *97*, uoad022.
[13] a) D. P. Arnold, *Polyhedron* **1986**, *5*, 1957–1963; b) D. P. Arnold, E. A. Morrison, J. V. Hanna, *Polyhedron* **1990**, *9*, 1331–1336; c) G. Smith, D. P. Arnold, C. H. L. Kennard, T. C. W. Mak, *Polyhedron* **1991**, *10*, 509–516; d) D. P. Arnold, J. Blok, *Coord. Chem. Rev.* **2004**, *248*, 299–319.
[14] Vaid discussed the antiaromaticity of **P1** based on the chemical shifts of the central ^{29}Si and peripheral ^{1}H nuclei. See, ref. [5].
[15] a) T. M. Krygowski, *J. Chem. Inf. Comput. Sci.* **1993**, *33*, 70–78; b) T. M. Krygowski, A. Ciesielski, C. W. Bird, A. Kotschy, *J. Chem. Inf. Comput. Sci.* **1995**, *35*, 203–210; c) M. K. Cyrañski, T. M. Krygowski, M. Wisiorowski, N. J. R. van Eikema Hommes, P. v R Schleyer, *Angew. Chem. Int. Ed.* **1998**, *37*, 177–180.
[16] D. M. Collins, W. R. Scheidt, J. L. Hoard, *J. Am. Chem. Soc.* **1972**, *94*, 6689–6696.
[17] D. P. Arnold, E. R. T. Tiekink, *Polyhedron* **1995**, *14*, 1785–1789.
[18] The assignment of the $C_{\beta1}$–H and $C_{\beta2}$–H signals of **2–X** were performed by nuclear Overhauser effect spectroscopy (NOESY).
[19] δ_{Sn} (ppm) of SnX_2TPP in $CDCl_3$: −621.1 (X = F), −589.7 (X = Cl), −631.1 (X = OBz), −569.6 (X = OH). See ref. 13.
[20] a) E. Steiner, P. W. Fowler, *Chem. Commun.* **2001**, 2220–2221; b) E. Steiner, P. W. Fowler, *J. Phys. Chem. A* **2001**, *105*, 9553–9562; c) N. S. Mills, A. Levy, B. F. Plummer, *J. Org. Chem.* **2004**, *69*, 6623–6633; d) T. Nishinaga, T. Ohmae, M. Iyoda, *Symmetry* **2010**, *2*, 76–97; e) P. W. Fowler, C. S. Anstöter, *ChemPhysChem* **2024**, *25*, e202300791.
[21] Y. Kudoh, E. Suzuki, H. Ochiai, K. Ise, Y. Kimura, M. Minoura, H. Nakano, Y. Matano, *Chem. Eur. J.* **2023**, *29*, e202302148.
[22] a) P. v R Schleyer, C. Maerker, A. Dransfeld, H. Jiao, N. J. R. van Eikema Hommes, *J. Am. Chem. Soc.* **1996**, *118*, 6317–6318; b) Z. Chen, C. S. Wannere, C. Corminboeuf, R. Puchta, P. v R Schleyer, *Chem. Rev.* **2005**, *105*, 3842–3888.
[23] R. Krishnan, J. S. Binkley, R. Seeger, J. A. Pople, *J. Chem. Phys.* **1980**, *72*, 650–654.
[24] a) P. J. Hay, W. R. Wadt, *J. Chem. Phys.* **1985**, *82*, 299–310; b) L. E. Roy, P. J. Hay, R. L. Martin, *J. Chem. Theory Comput.* **2008**, *4*, 1029–1031; c) C. E. Check, T. O. Faust, J. M. Bailey, B. J. Wright, T. M. Gilbert, L. S. Sunderlin, *J. Phys. Chem. A* **2001**, *105*, 8111–8116.
[25] a) A. D. Becke, *J. Chem. Phys.* **1993**, *98*, 5648–5652; b) C. Lee, W. Yang, R. G. Parr, *Phys. Rev. B* **1988**, *37*, 785–789.
[26] E. Cancès, B. Mennucci, J. Tomasi, *J. Chem. Phys.* **1997**, *107*, 3032–3041.
[27] a) W. J. Hehre, R. Ditchfield, J. A. Pople, *J. Chem. Phys.* **1972**, *56*, 2257–2261; b) P. C. Hariharan, J. A. Pople, *Theor. Chim. Acta* **1973**, *28*, 213–222; c) T. Clark, J. Chandrasekhar, G. W. Spitznagel, P. v R Schleyer, *J. Comput. Chem.* **1983**, *4*, 294–301; d) V. A. Rassolov, J. A. Pople, M. A. Ratner, T. L. Windus, *J. Chem. Phys.* **1998**, *109*, 1223–1229.
[28] M. J. Frisch, G. W. Trucks, H. B. Schlegel, G. E. Scuseria, M. A. Robb, J. R. Cheeseman, G. Scalmani, V. Barone, G. A. Petersson, H. Nakatsuji, X. Li, M. Caricato, A. V. Marenich, J. Bloino, B. G. Janesko, R. Gomperts, B. Mennucci, H. P. Hratchian, J. V. Ortiz, A. F. Izmaylov, J. L. Sonnenberg, D. Williams-Young, F. Ding, F. Lipparini, F. Egidi, J. Goings, B. Peng, A. Petrone, T. Henderson, D. Ranasinghe, V. G. Zakrzewski, J. Gao, N. Rega, G. Zheng, W. Liang, M. Hada, M. Ehara, K. Toyota, R. Fukuda, J. Hasegawa, M. Ishida, T. Nakajima, Y. Honda, O. Kitao, H. Nakai, T. Vreven, K. Throssell, J. A. Montgomery, Jr., J. E. Peralta, F. Ogliaro, M. J. Bearpark, J. J. Heyd, E. N. Brothers, K. N. Kudin, V. N. Staroverov, T. A. Keith, R. Kobayashi, J. Normand, K. Raghavachari, A. P. Rendell, J. C. Burant, S. S. Iyengar, J. Tomasi, M. Cossi, J. M. Millam, M. Klene, C. Adamo, R. Cammi, J. W. Ochterski, R. L. Martin, K. Morokuma, O. Farkas, J. B. Foresman, D. J. Fox, Gaussian 16, Revision C.01; Gaussian, Inc., Wallingford CT, 2019.
[29] S. Stoll, A. Schweiger, *J. Magn. Reson.* **2006**, *178*, 42–55.

Manuscript received: November 5, 2024
Accepted manuscript online: December 13, 2024
Version of record online: December 27, 2024